In-Situ Ice Adhesion Testing using the Deformed Skin Adhesion Test

Christopher Giuffre[1]
HX5, LLC, Cleveland, Ohio 44142 USA

There exists a plethora of ice adhesion testing methods such as centrifuge-based methods, push/pull methods, and lap joint shear tests. However, these methods often cannot be done in-situ during an icing spray and require researcher handling/preparation prior to testing. Additionally, many of these methods test ice accretions that are not representative of the ice shapes that grow on airframes which can have unintended consequences such as edge or corner stress concentrations. In order to mitigate the issues present with other ice adhesion tests, a novel, hands-free, in-situ test method imbedded into the leading edge of an airfoil has been developed and tested in the NASA Glenn Research Center's Icing Research Tunnel. The mechanics of the new test method are discussed with finite element simulations being used to highlight the fundamental mechanics of this test method. The testing procedures used during the experimental test campaign are discussed along with the icing cloud test matrix. Analysis of the force-displacement results highlights the repeatability of the test method with regards to both sample behavior across several days of testing and different ice shapes. The results from the first run of the day showed a significant discrepancy from subsequent runs and differential image analysis was used to determine differences in the interfacial bonding states between runs.

I. Nomenclature

AOA	=	Angle of Attack
LWC	=	Liquid Water Content
mm	=	Millimeter
MVD	=	Median Volumetric Diameter
N	=	Newton
PSI	=	Pounds per Square Inch
t_{ice}	=	Ice Layer Thickness
u_y	=	Y Component of Displacement
σ_{yy}	=	Tensile Opening Stress
Hz	=	Hertz

II. Introduction

Despite over 80 years of study, the mechanical testing of impact ice bonded to substrates remains an active area of research [1]. These measurements are critical to the future of aviation safety as the data gathered from these experiments will become the necessary inputs to simulations that will predict ice shedding for both aircraft airframes as well as rotating propulsors. The need to accurately measure the adhesive strength of the interface has led to the development of a large variety of tests such as push tests, zero-degree cone tests, modified lap shear tests, and centrifugal methods [2]. Due to the differences in the way each method generates the critical interfacial tractions required to induce delamination, direct comparison between different tests remains difficult [3]. Additionally, the

[1] Aerospace Engineer, 21000 Brookpark Rd. Cleveland, OH, 44135

lack of a recognized standard for ice adhesion testing has further exacerbated the problem of direct comparison between experimental facilities as even tests within the same family might be conducted differently [3].

Beyond the lack of standardization, another prevalent issue within the field of ice adhesion is that few methods are completely hands-off and can be conducted inside of an icing wind tunnel. Of the methods studied in a recent round-robin interlaboratory comparison test campaign [4], nearly all the testing techniques required handling prior to testing, which has the potential to induce damage into the interface that cannot be readily characterized. While efforts have been made to minimize the impact of sample transportation between icing wind tunnel and testing facility [5], this remains an issue which likely leads to the large spread in the reported adhesion measurements. Most of the hands off testing techniques are either specialized fracture mechanics based experiments [6] or are centrifugal methods [7] which have their own set of difficulties when comparing results with more common adhesion test methods. Lastly most ice adhesion tests are done on small coupons, which produce impact ice geometries which are not representative to the ice shapes observed on aircraft in flight.

To provide a consistent methodology for conducting ice adhesion testing, the deformed skin adhesion test (DSAT) [8] was conducted in-situ during an icing spray in the NASA Glenn Research Center (GRC) Icing Research Tunnel (IRT) [9]. Imbedded into the leading edge of the 65% Midspan section of the hybrid Common Research Model (CRM) [10], the test article is instrumented to measure the force and displacement applied to the test article that correspond to the generation of the necessary surface tractions to promote interfacial delamination. Tests were conducted in the IRT over several days with runs being conducted both while the icing cloud was being sprayed and with the tunnel brought down to idle. Finite element simulations support the experimental work to better understand the fundamental mechanics of the test.

III. Methodology

A. Methodology for Generating Delamination Tractions

Unlike most ice adhesion test methods which rely on deforming the ice accreted on a rigid substrate to generate the needed surface tractions to induce delamination, the DSAT introduces the critical surface tractions by deforming the underlying substrate. To achieve this, the DSAT consists of 3 main components as highlighted in the cutaway view shown in Fig 1. The coupon serves as the collection substrate for the impact ice and is exposed directly to the cloud of the IRT. Mounted directly in the center of the coupon, the rod is pulled in the spanwise direction to deform the coupon. This bending of the rod will induce the interfacial tractions to delaminate the interface between coupon and accreted ice. Lastly, the end supports are attached to the skin and allow for mechanical attachment to a frame that will support the coupon and contains the instrumentation within the leading edge of the CRM wind tunnel model.

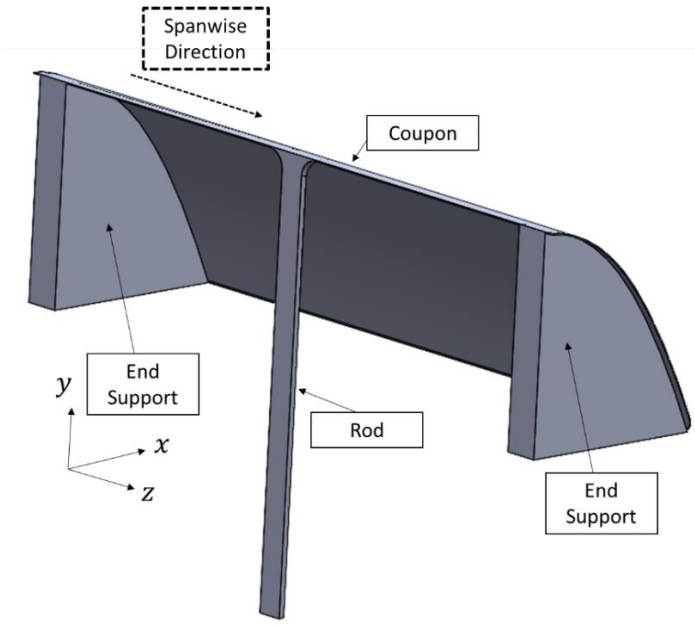

Fig. 1 DSAT components

To highlight the fundamental principles and mechanics of the DSAT, a simplified finite element model was constructed using Abaqus/CAE 2022. The end supports are modeled using fixed boundary conditions as shown in Fig. 2, with the ice layer in light blue and the DSAT in gray. The DSAT was designed to stay within the linear elastic regime of Grade 5 Titanium with a Young's Modulus of $E = 114\ GPa$ and a Poisson's Ratio of $\nu = 0.3$. The ice layer is assumed to have a Young's Modulus of $E = 9.8\ GPa$ and a Poisson's Ratio of $\nu = 0.3$ [11]. The deformation of the DSAT coupon is induced by specifying displacement in the spanwise (-z) direction to the bottom of the rod, and this can be seen in Fig. 2. This was done to reduce computational time and this assumption is sufficient for the analysis presented in this work. The outer mold line of the coupon was defined by fitting a 5th order polynomial to the leading-edge outer mold line of the CRM and then the polynomial was discretized into 50 linear segments to improve meshing and provide a well-defined series of surfaces. The coupon has a constant thickness of 0.4 mm, matching the physical test article. The use of a single analytically defined spline function to define the outer mold line was investigated but provided inferior results to the linear segment model. This step was taken to ensure a perfect match along the interface between the coupon and ice layer. For the purposes of this work, no fracture mechanics modeling was included in the simulation efforts and the interface was defined using the surface-to-surface tie constraint capability of Abaqus. This constraint type relieves the requirement of having matching meshes along the interface, which allows for part specific mesh refinement in the areas of high stress such as the coupon near the rod attachment point. The ice layer was modeled to have a constant thickness and covers a sufficient area of the coupon such that there are no finite size effects from the length and width of the ice layer [8]. To ensure a mesh convergence, the adaptive remeshing capability of Abaqus was used on the elements along the interface. The von Mises stress was selected as the error indicator variable, with the default values for the sizing method and constraints being used. The entire model was meshed with linear tetrahedral C3D4 elements and solution convergence was achieved within 3 mesh refinement steps for all cases presented.

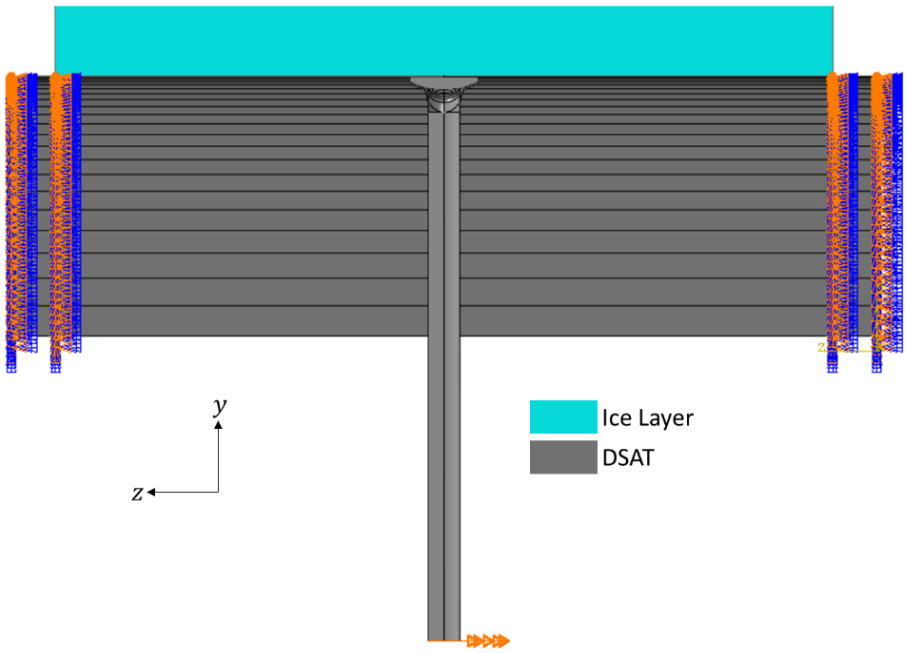

Fig. 2 DSAT boundary conditions and loading configuration

The deformation was induced in the DSAT simulations by applying a 5 mm displacement in the negative z direction is shown in Fig. 3. The view shown is from a cut made along the leading edge of the airfoil, which will expose the region experiencing the largest deformation and stresses. The deformation of the entire model is shown using a scale factor of 5x while the area near the top of the rod is shown at 50x scale factor. The resulting u_y displacement field and σ_{yy} stress fields are given in Fig. 4 on the undeformed shape to improve visualization. Although the applied displacement is in millimeters, the maximum displacements seen along the interface are in the order of tens of micrometers. However, this is a sufficient displacement to generate more than the required stresses to induce delamination [3]. This change in the scale of the displacements will allow for a very gradual increase of the interfacial stresses, allowing for a high degree of control when loading the interface. The σ_{yy} stress field was selected as the

primary stress field of interest due to it being the Mode I (tensile) opening stress along the interface and the highest stress component the interface is expected to experience. All subsequent finite element field plots will be on the undeformed shape. Due to the bending of the rod, the Mode I opening stresses and displacement field are inversely related. Additionally, the extent of the displacement field is much larger compared to the stress field which is due to the inability of the upper surface of the ice to support σ_{yy} due to it being a free surface in that direction.

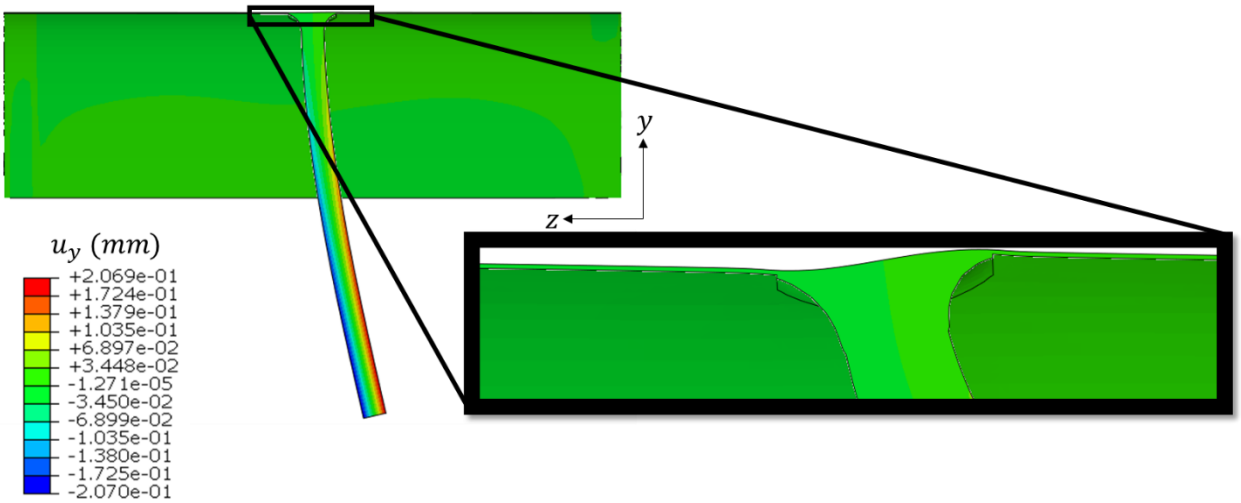

Fig. 3 Coupon deformation

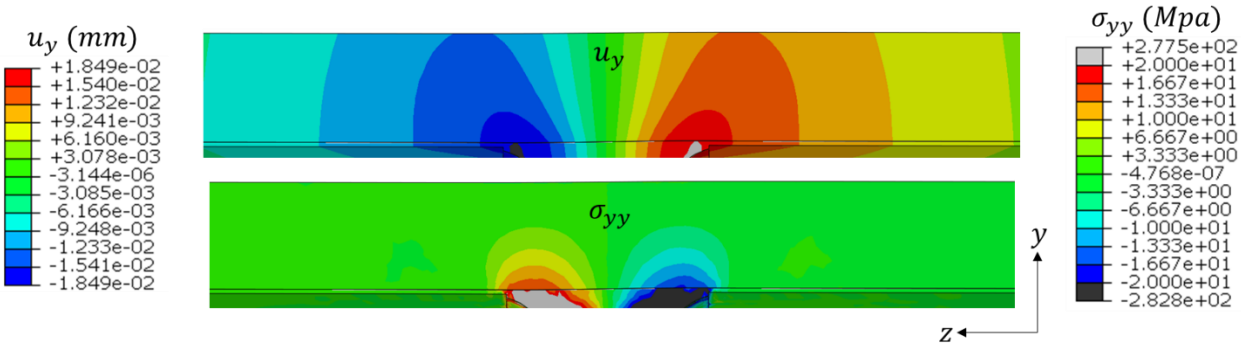

Fig. 4 Opening displacements and stress in the ice layer due to coupon deformation

With the interface being modeled as a tie constraint, the displacement field is continuous across the interface while the stress is not due to the elastic mismatch between the DSAT and ice layer. Additionally, the drop in Young's Modulus across the interface from the DSAT to the ice layer means that, while the primary stress driving delamination will be σ_{yy}, all components of stress will be present along the interface. This is highlighted in Fig. 5 where the interfacial stress distributions are shown for all 6 stress components. The footprint of the rod is overlaid on each stress field to highlight the localized concentration of stresses in this test method. The only other significant stresses present are a secondary opening stress, σ_{zz}, as well as the shear stress of the two primary opening modes, σ_{yz}. Both are approximately a third of the magnitude of σ_{yy}, which means the additional stress components will only have a modest impact on the total fracture energy of the interface and the test can be considered Mode I dominate [12].

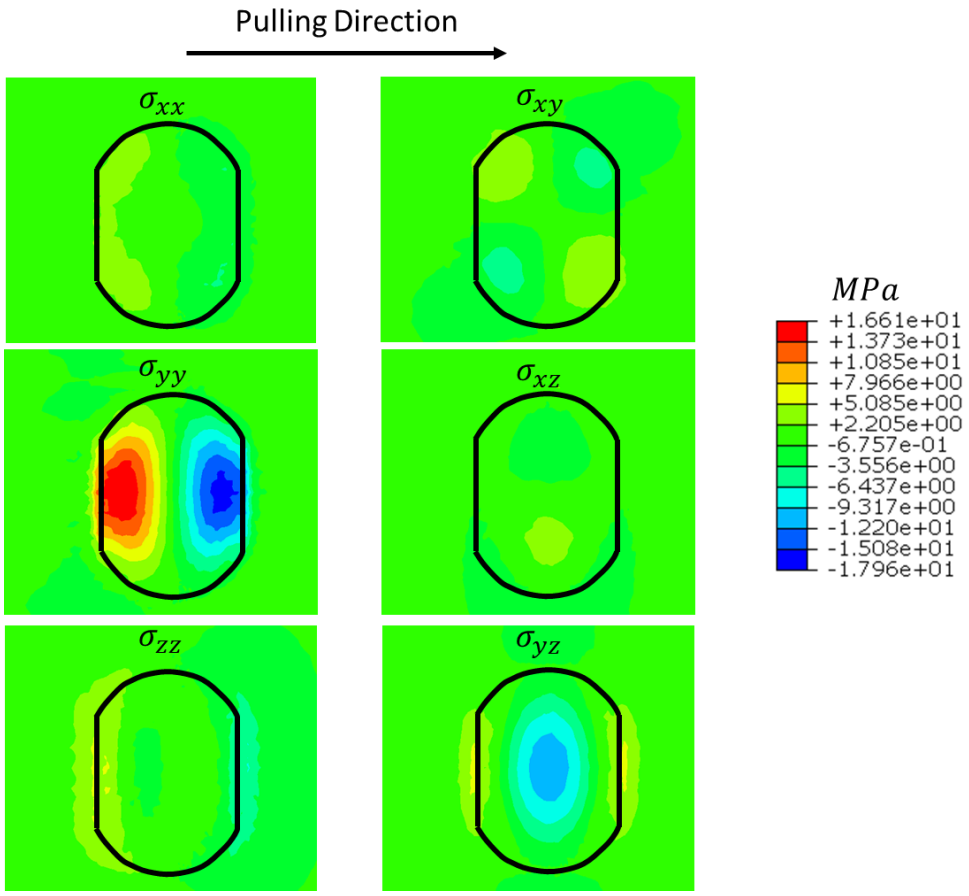

Fig. 5 Stresses present on the ice interface during loading

Finally, the role of ice layer thickness was studied as this will be a key parameter in the experimental portion of this work. Due to the configuration of the DSAT and the method for generating the critical tractions, the stresses in the ice layer quickly diffuse into the bulk material and the ice away from the rod attachment point will be stress free. With this in consideration, there is a critical thickness above which there will only be slight variations in the measured response of the system to loading during the experiment [13]. The σ_{yy} opening stress distributions from simulations with ice thickness of five, ten, and twenty millimeters is shown in Fig. 6 to demonstrate this behavior. By plotting all three simulations on the same scale, it is clear that the $t_{ice} = 5\ mm$ ice does not develop the same stress field as the ten- and twenty-millimeter thick ice layers. This implies that after 10mm of ice growth, any additional ice growth will have minimal influence on the measured force required to induce the same displacement.

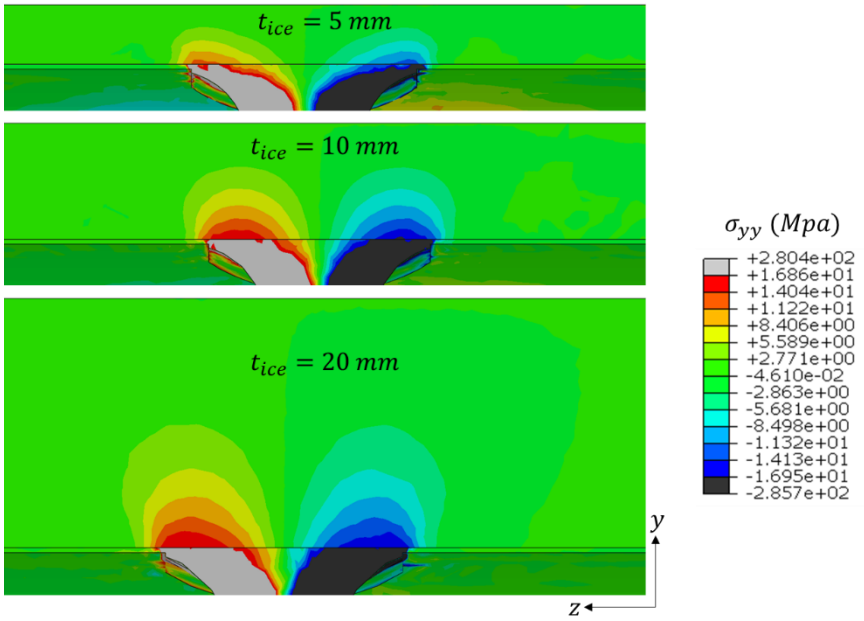

Fig. 6 Role of ice layer thickness on σ_{yy}

B. Coupon Fabrication and Test Article Instrumentation

The DSAT test article was fabricated out of Grade 5 Titanium alloy and consists of the coupon, rod, and end supports as shown in Fig. 7. The rod has been vacuum-brazed to the coupon where the metallurgical bond ensures effective transfer of displacement from the rod to the coupon. The endplates were laser welded directly to the coupon which provide the fixed boundary condition. Waviness along the edges of the coupon occurred during the welding of the end supports to the coupon and were corrected by laser welding small titanium runners along the length of the DSAT. These were not considered during the simulation portion of this work as that region of the DSAT does not experience any significant stress during a test. The test article and accompanying frame that contains the instrumentation are shown in Fig. 8. The DSAT is attached to this frame via 4 bolts, two in each end support, which prevent the DSAT from moving during a wind tunnel run and subsequent delamination experiment. Two pieces of instrumentation from Omega Engineering are contained with the frame to record the test article response to loading: a single-axis 100 pound-force capacity LCCD load cell to record the applied load and a linear variable inductance transducer (LVIT) to record the displacement applied to the rod [13]. The displacement is applied to the rod via a dynamic, high-resolution, linear ball screw driven linear actuator also attached to the testing frame. Both pieces of instrumentation and the linear actuator are IP67 rated which will enable them to survive the conditions present inside of the model during wind tunnel operation. By measuring both the displacement applied to the rod and the resulting force, the overall behavior of the system can be characterized by the system stiffness which is the slope of the force-displacement curve generated during an experiment. Using this instrumentation set-up, any delamination events occurring along the interface will be readily identifiable since they will result in a change in the applied load required to hold a specific displacement. This will also allow for the extent of the delamination to be better understood since if the sample is delaminated to the extent where the ice is no longer stressed, the stiffness will be the same as if an experiment was conducted without an ice accretion.

Fig. 7 DSAT test article

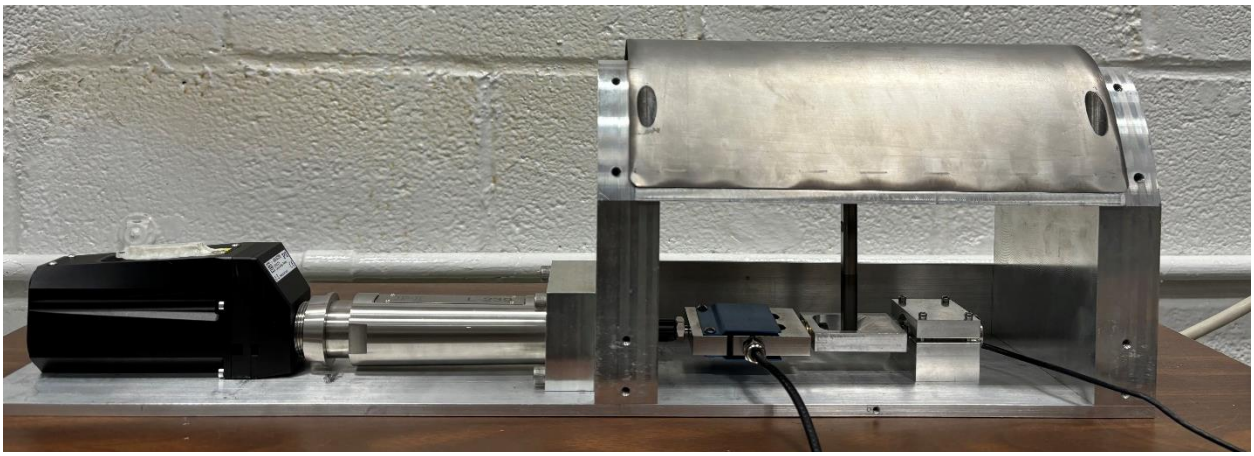

Fig. 8 DSAT test article and support frame

The leading edge portion of the CRM model was modified with a cut out the same size as the DSAT coupon to enable continuous exposure to the icing environment. The frame was then attached to the leading edge via a total of 8 screws, 4 at each end, which prevent undesired movement of the DSAT during testing. After installation of the leading edge with the DSAT attached, aluminum tape was used to close the seams between coupon and leading edge to prevent liquid water reaching the instrumentation within the airfoil. This both protected the electronics attached to the frame along with minimizing any disturbances to the flow due to modification of the airfoil. A front and side view of the DSAT fully installed in the IRT is shown in Fig. 9. Although the edges of the coupon are not completely flush with the leading edge, they are sufficiently far away from the center of the DSAT that any deviations of ice accretion around the coupon edges will be negligible and not require consideration when analyzing the experiment. The Solidworks model in Fig. 10 shows the location of the DSAT in the full CRM model. Due to internal structure of the existing CRM model, the DSAT could not be centered vertically in the test section. However, the entirety of the coupon remains well within the calibrated region of the IRT [9].

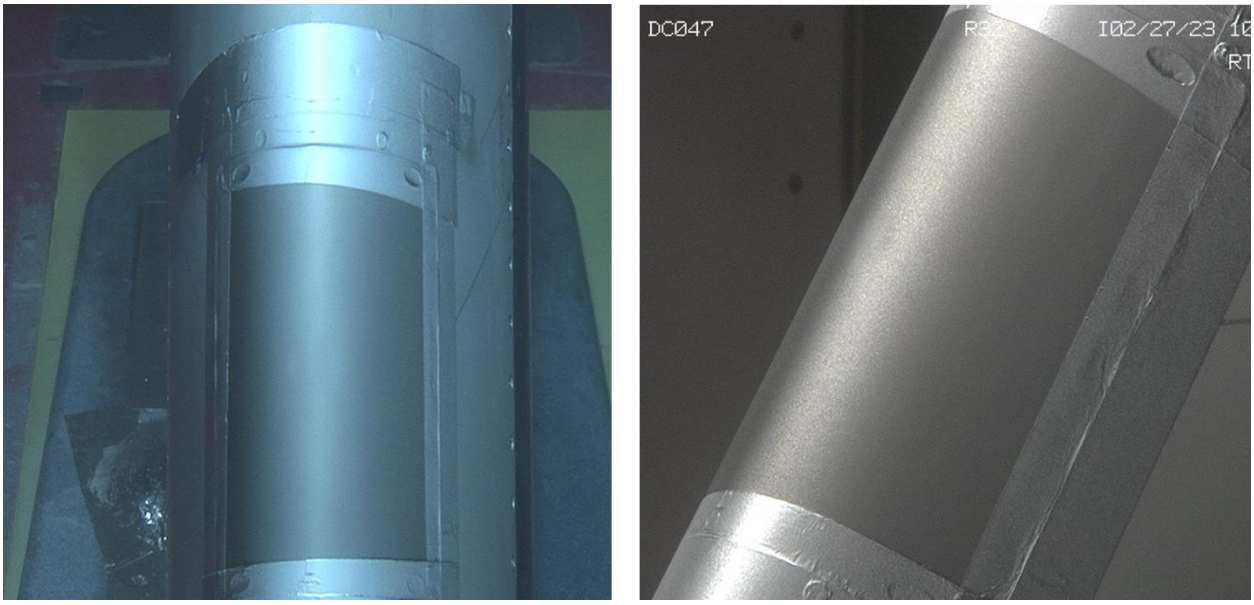

Fig. 9 DSAT installed into CRM

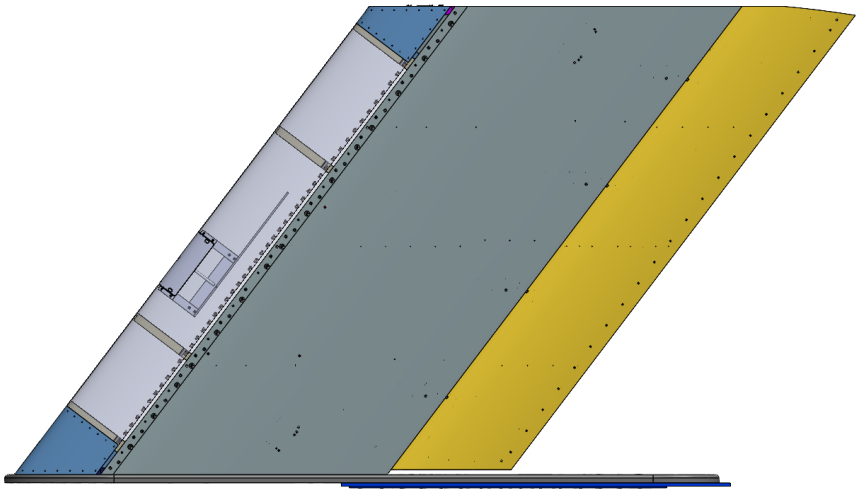

Fig. 10 Rendering of the location of the DSAT within the CRM

C. IRT Test Matrix and Testing Procedures

The focus of this test campaign was on rime icing conditions since this icing regime results a near constant spanwise cross section. This is critical as geometric variations such as scallop ice shapes could result in unexpected traction distributions along the interface. A total of 15 adhesion tests were conducted, with the full test matrix given in Table 1. The cloud conditions were held constant across all runs while the spray time and angle of attack were altered for select tests.

Table 1 IRT Test Campaign Icing Cloud Matrix

Run ID	Spray Time (min)	AOA (Deg)	Total Air Temp (Deg. C)	True Air Speed (Knots)	MVD (micron)	LWC (g/m^3)	Air Press. (PSI)	DPRESS H_20 (PSID)	Nozzle Type
TH3654	15.0	0.0	-14.8	150	25.0	0.70	12.7	35.3	Mod1
TH3655	20.0								
TH3658	15.0								
TH3660	20.0								
TH3661	15.0	1.0							
TH3662	20	0.0							
TH3663									
TH3664									
TH3667									
TH3668									
TH3669									
TH3670									
TH3671									
TH3672									
TH3673									

All the tests were conducted at a constant applied displacement rate of 50 micrometers per second. This applied displacement rate was selected so that the delamination would be a noticeable event given a sampling rate of 250 Hz that could be achieved using the instrumentation. To minimize the impact of noise on the results, a 50-point moving average was used to smooth the data and all force-displacement results presented in this work is the smoothed data. Additionally, starting with Run ID TH3668, the experiment was conducted with 2 minutes and 30 seconds remaining in the spray to study the effects of residual stresses on the systems response to loading [14]. It was determined that any ice accreted beyond 15 minutes of spray time did not alter the response of the sample to loading, which allows for direct comparison of these runs with the 20-minute post spray experiments. After each test, the ice was removed from the model and the coupon was cleaned with 99% isopropanol alcohol to remove any contamination on the testing interface. No equilibration spray was conducted at the start of each day of testing.

Prior to the start of testing each day the DSAT was tested to establish the baseline stiffness, hereafter referred to as the "Dry Pull." This was done to ensure the DSAT would perform as expected during testing as well as alert the research team to any permanent damage incurred during the previous days testing. Additionally, the DSAT was 3D scanned before each day of testing and compared with the scans taken earlier in the test campaign to determine if any permanent deformation had occurred to the coupon. Over the duration of the test campaign, no appreciable change in the outer mold line geometry of the DSAT was observed and the results from each dry pull test were very similar to the measurements made on the other testing days. To ensure no preloading of the coupon during an icing spray, the linear actuator was extended such that no applied load was measured. Due to the relatively slow displacement rate of the test, there was no observable jump or backlash in the force-displacement results when the pulling fixture comes into contact with the rod. The starting position of the linear actuator prior to each test was recorded as a secondary check to ensure no plastic deformation of the DSAT had occurred in the previous run. Results from a "Dry Pull" test are given in Fig. 11 with DSAT producing a linear force-displacement plot as expected since the system was designed to operate entirely in the elastic deformation regime of titanium. The noise observed during a "Dry Pull" was consistent with what was observed during adhesion tests and does not influence the interpretation of the results from testing.

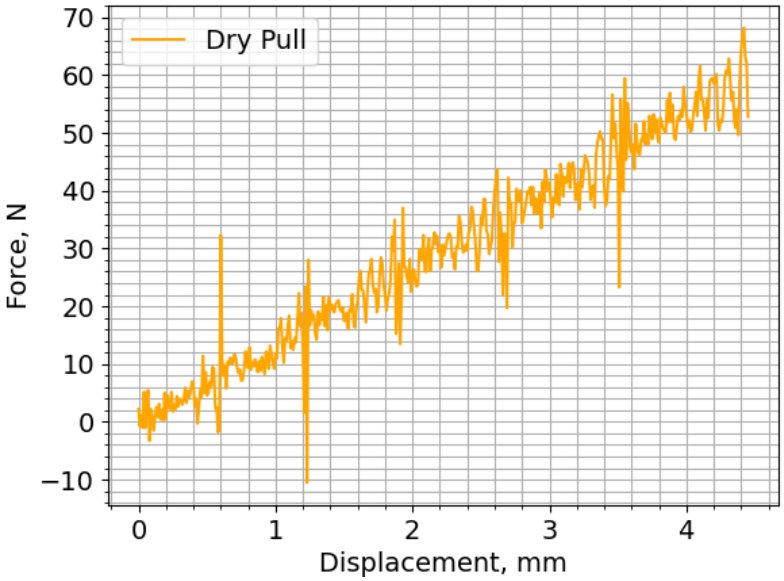

Fig. 11 "Dry Pull" results

IV. Results

A. Experimental Force-Displacement Response

The results from Run ID TH3669 are shown in Fig. 12a where there is a period of initial linear loading followed by a small period where the response plateaus at around 3.2mm of displacement then another period of linear loading until the end of the experiment. To better analyze these regions of the experiment, linear regressions were conducted in the regions where the interface was intact, and after a change in response was noted in what is referred to as the post break region. The results from fitting both regressions are overlaid with the gathered experimental data and shown in Fig. 12b. The initiation of delamination occurs within the yellow highlighted area of Fig. 12b which corresponds to 1 second. For the experiments conducted during this campaign, only a single delamination event was observed during each test which insinuates the delamination propagated sufficiently large enough such that the ice layer no longer experiences any stresses due to deformation of the coupon. This is confirmed in Fig. 13 where the post-break behavior of the DSAT is very similar to that of the "Dry Pull" conducted prior to that day of testing. The increase in stiffness in the DSAT due to the accreted ice can also be seen in Fig. 13 as the stiffness of the DSAT prior to delamination is higher than the "Dry Pull."

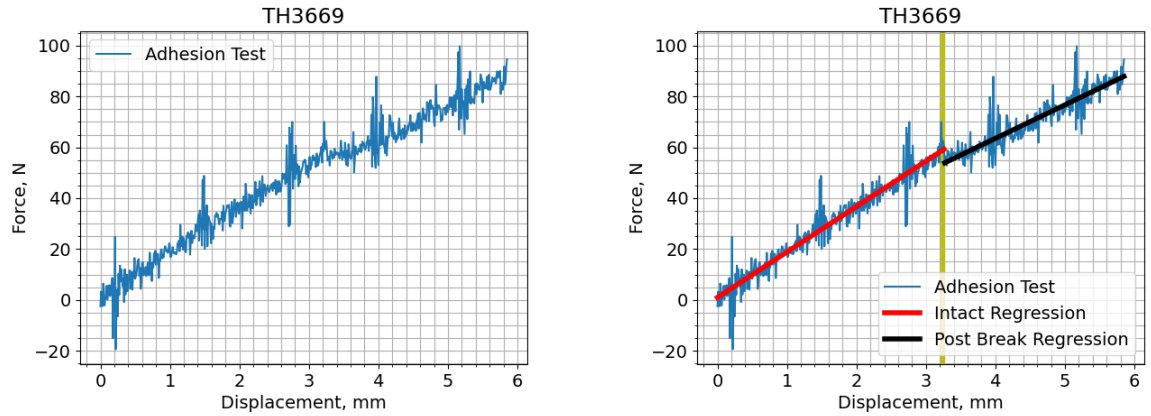

Fig. 12 DSAT results with an ice accretion

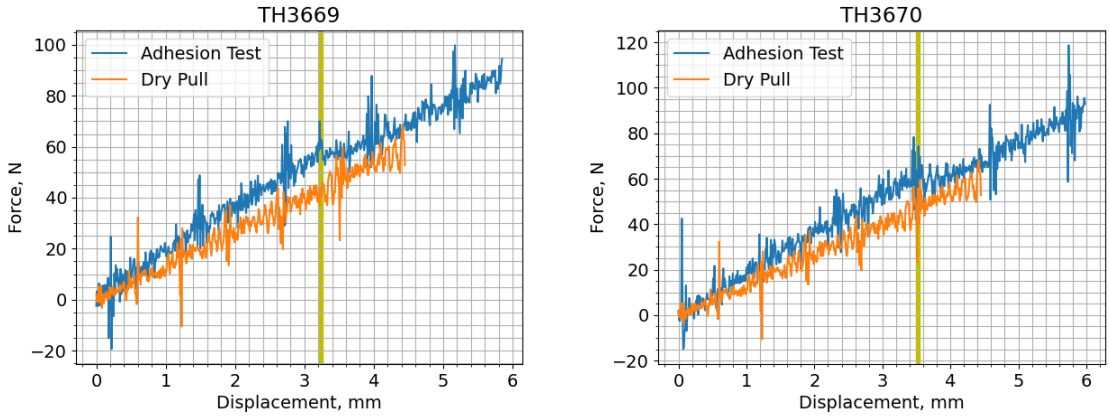

Fig. 13 Comparison of adhesion test results with "Dry Pull"

B. DSAT Repeatability

Since the DSAT is a completely hands-off adhesion test, it has the potential to significantly improve repeatability over past adhesion test campagins [5]. This is confirmed by plotting the slope calculated from fitting a linear regression to the stiffness results gathered on the fifth day of testing in Fig. 14 with the error bars showing the standard error on the estimated slope. Examination of the results from runs TH3668 through TH3673 confirm the DSAT as a candidate ice adhesion test capable of producing highly repeatable adhesion test results. All of these tests were conducted while the IRT was still spraying the icing cloud, with the adhesion tests starting at 2:30 remaining in the spray duration. Only run TH3672 presents a slightly elevated stiffness while the interface is intact than the other tests, but this can be attributed to run to run variation within an icing tunnel. There is significantly more varation in the post-break regression analysis, but all of the results are close to the stiffness measured at the start of day "Dry Pull" run.

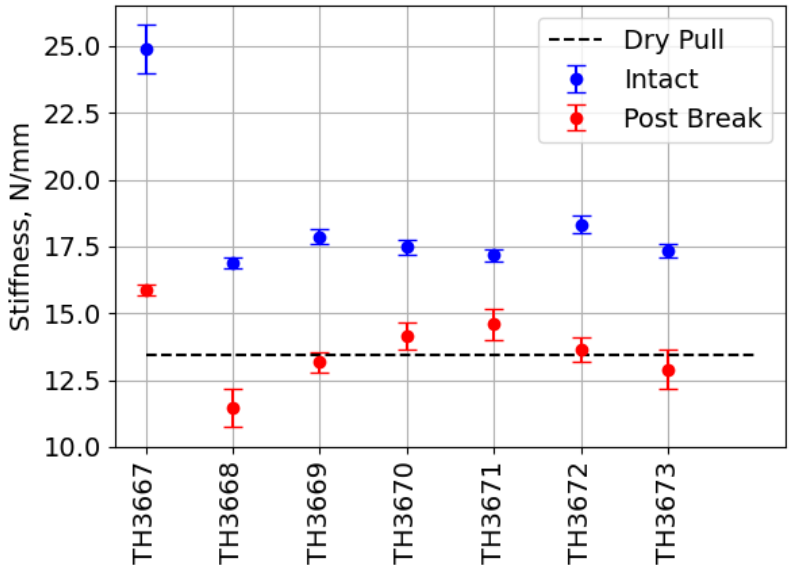

Fig. 14 All Stiffness Fitting Results from a Single Day of Testing

The only run from this day of testing that exhibits a significant deviation in stiffness prior to delamination is run TH3667 which was the first run conducted during that day of testing. The testing procedures were identical to all other tests conducted during the day, and the icing conditions for all tests were identical. With testing starting after 17.5 minutes of ice accretion, an already sufficiently thick ice layer had been accreted to produce ice-shape independent results. As a result, the only explanation for this anomaly is a change in the state of the ice bonding to the interface during accretion. To determine if there are any differences along the interface between the DSAT and ice layer, differential image analysis was conducted on a set of images taken from the recordings made during each testing spray. This is accomplished by selecting an image taken immediately after the spray began, and then subtracting this image from an image taken later in the test. The reference images for both a side and top view along with images taken 30 seconds into the spray duration are shown in Fig. 15 (a-d). The shiny band located near the stagnation point of the airfoil is due to the lighting set-up used during this testing and does not indicate any damage along the interface. The results of subtracting Fig. 15a from Fig. 15c is given in Fig. 15e, and Fig. 15b from Fig. 15d is given in Fig. 15f. Based on this analysis, there is no indication of damage present anywhere on the interface for run TH3667.

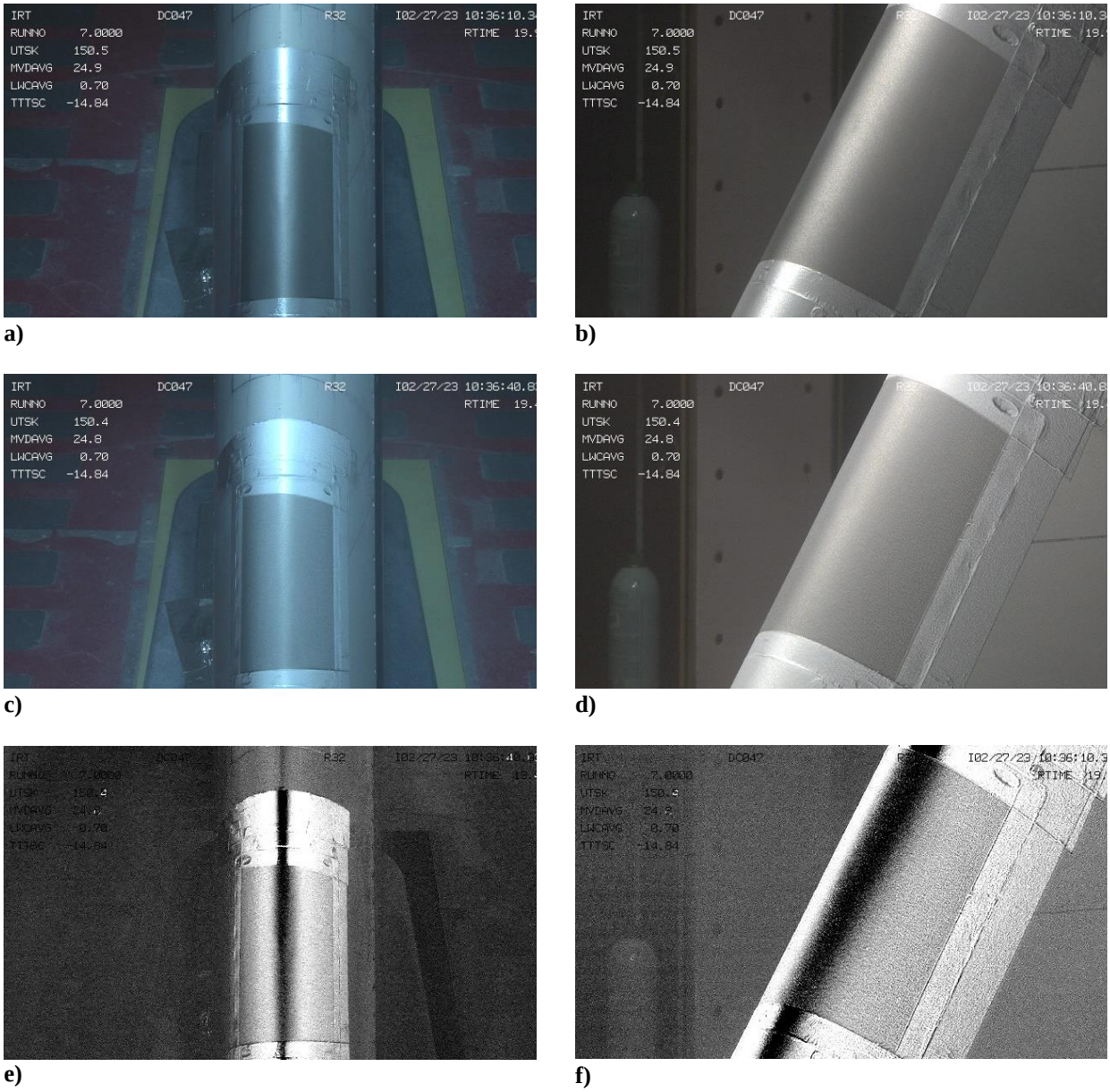

Fig. 15 Initial ice growth on the DSAT coupon after 30 seconds of spraying from run TH3667: a) front reference image, b) side reference image, c) front image 30 seconds into spray, d) side image 30 seconds into spray, e) difference between a) and b), f) difference between b) and d)

However, this is not the case when conducting the same analysis on run TH3668, the subsequent run from that day of testing. In this case, both Fig. 16e and Fig. 16f show different results when compared with the differential images in Fig. 15. This is a clear indication of a change in the state of the interface between the ice and DSAT coupon which will then affect the results from the adhesion test. This change in behavior occurs in the center of the coupon, where the rod is attached to the coupon. A visual examination of the test article inside of the tunnel after a 30 second spray appeared to show that this was the only location on the coupon where it appeared the ice had bonded to the DSAT test article. A change in bonding from the full test article to a small location in the center provides a sufficient explanation to the significant drop in measured stiffness from the first run and all subsequent runs. Due to this, the adhesion strength of the interface could not be determined at this time as exploring this anomaly will require significant simulation efforts which are beyond the scope of this work.

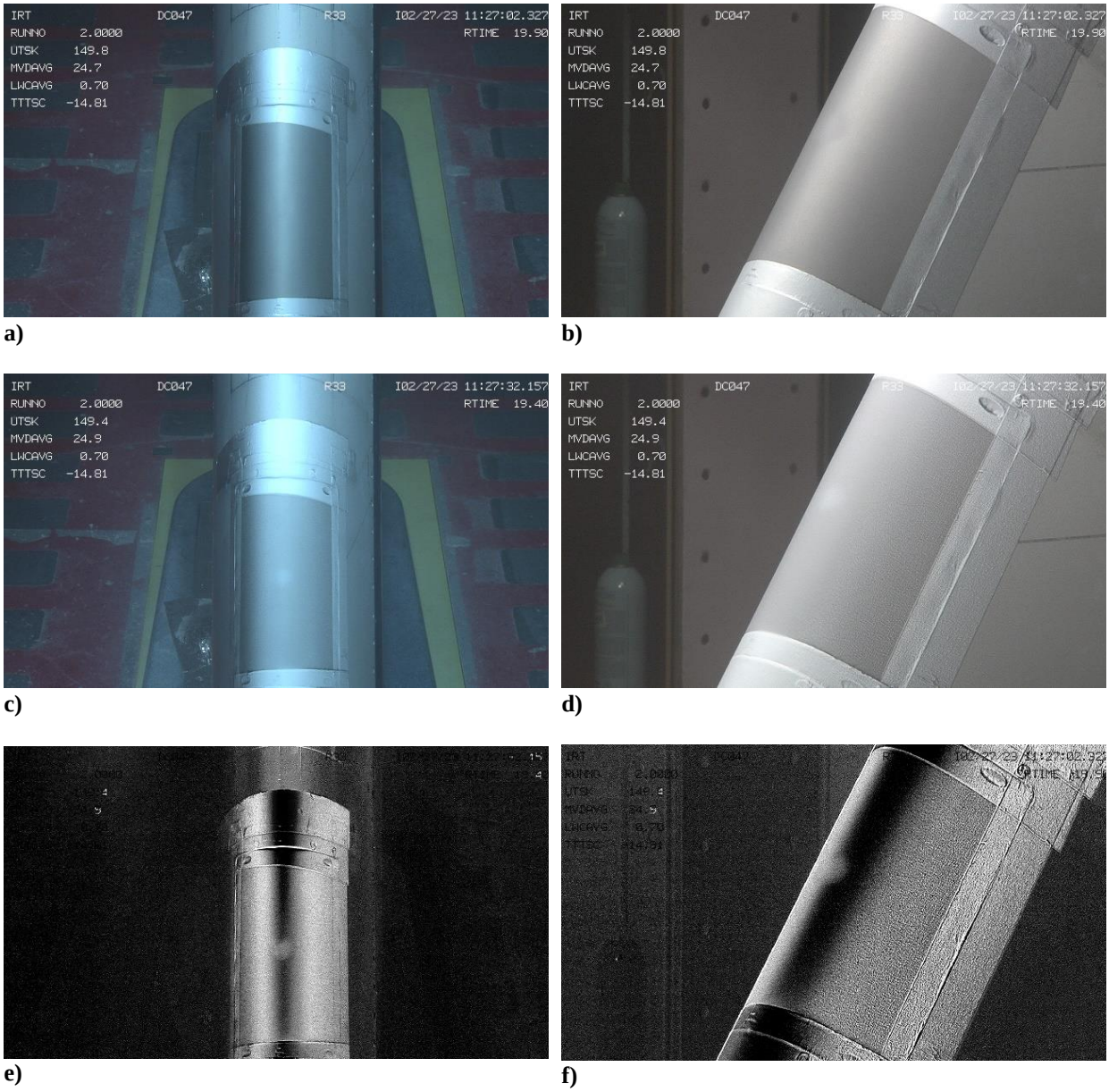

Fig. 16 Initial ice growth on the DSAT coupon after 30 seconds of spraying from run TH3668: a) front reference image, b) side reference image, c) front image 30 seconds into spray, d) side image 30 seconds into spray, e) difference between a) and b), f) difference between b) and d)

V. Discussion

The results from fitting the intact and post break stiffnesses from all DSAT runs documented in Table 1 are given in Fig. 17 along with a comparison of each day with the "Dry Pull" test conducted prior to the start of testing each given day. For all three days of testing reported, the first run of each day of testing present a much higher initial stiffness as discussed in the previous section: TH3654, TH3660, and TH3667. Efforts were made to try and replicate the first run of the day results in subsequent tests such as warming the DSAT to room temperature before starting the next test run. However, this did not produce similar results to the first test of the day. There were no significant

anomalies in the monitoring data gathered from the IRT to indicate that the tunnel was running off the conditions specified in Table 1. The root cause of this anomaly and its consequences on further analysis of the DSAT results requires further investigation. The differences in the post break regression analysis are likely due to the assumption that the delamination happened near instantaneously along the interface. The delamination process takes some time to occur, which means a small set of data needs to be excluded from the post break regression analysis. This will be considered during future analysis but was seen as an appropriate assumption for the level of analysis presented in this work.

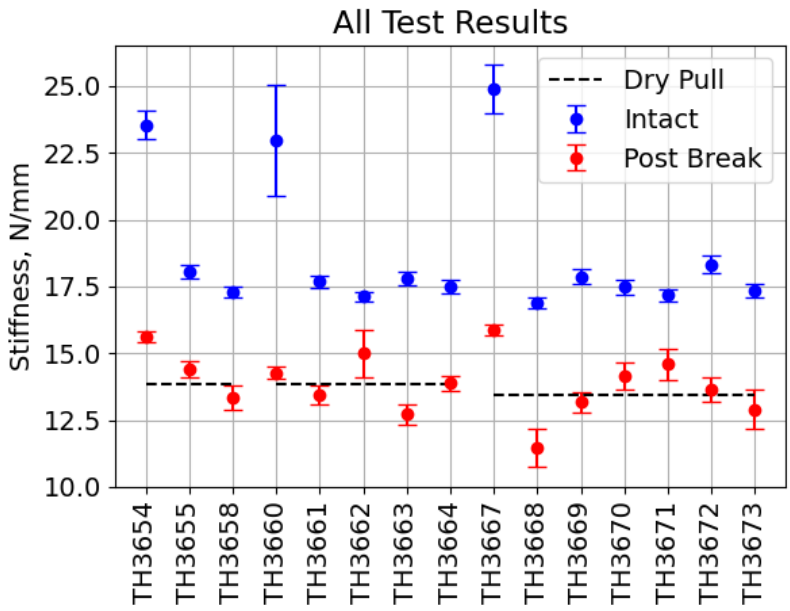

Fig. 17 DSAT repeatability with the "Dry Pull" stiffness denoted with the black dashed line

The maximum load applied to the DSAT prior to the delamination event was also recorded for each experiment and shown in Fig. 18, with the failure load being shown is the maximum force value from the intact regression. This was done to minimize ambiguity introduced into the analysis caused by directly interpreting the recorded force-displacement results since they often contain noise spikes near the delamination event. The first runs of the day show a significant deviation from the majority of test results, another indication that the interface was not at the same state for all of the tests. Additionally, the applied load shows significantly more run-to-run variation compared to the stiffness results, meaning that there remains some of the run-to-run variability that plagues ice adhesion research. However, most of the tests produced a failure load within an 8 N band which is an improvement over previous ice adhesion testing efforts. Individual simulations of the DSAT to these applied loads will reveal the true extent of the spread on the adhesion strength, but this initial analysis shows the DSAT can produce repeatable adhesion results.

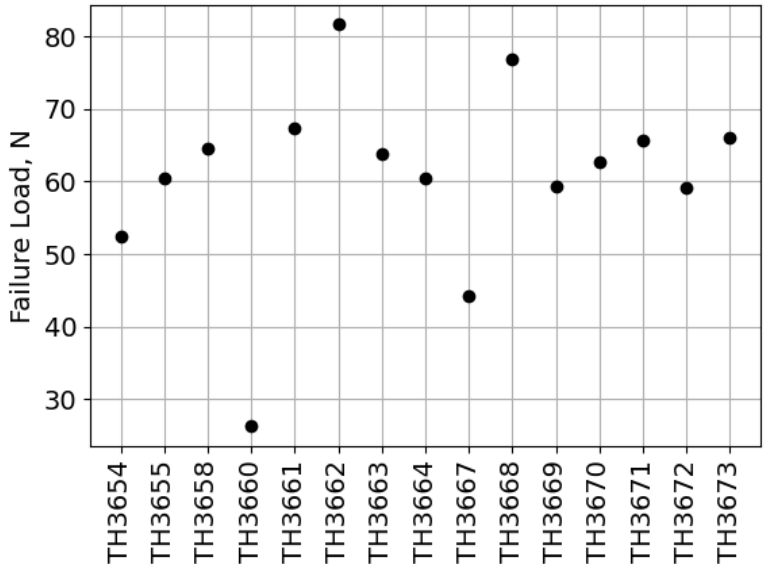

Fig. 18 Applied load required to induce delamination

Additionally, it appears that residual stresses induced along the interface during accretion have no impact on the global behavior of the DSAT. Starting with run TH3668, the tunnel was running on condition when the adhesion test was performed, and the results do not differ from tests conducted after the tunnel had been brought down to idle. The primary reason being this is a normal opening stress dominated test, and the associated residual strains were not measured in previous IRT test campaigns [14]. If the out-of-plane residual strains is on the same magnitude of the in-plane strains measured in 2021, there is negligible effects on the outcome of this experiment.

As expected based on the finite element results, the ice shapes tested in this test campaign led to the stiffness results from the DSAT being independent of the shapes of the ice accretions. The five ice shapes tested are shown in Fig. 19 and this indicates that additional ice accreted while the adhesion test was occurring has no effect on the measurements taken during testing. For those cases, the largest ice shape will be used in future work as the representative ice shapes from those cases. The changes in width (extent in the Y direction) of the ice accretions will not have any effect as the stresses generated are localized to the position where the rod was brazed onto the coupon.

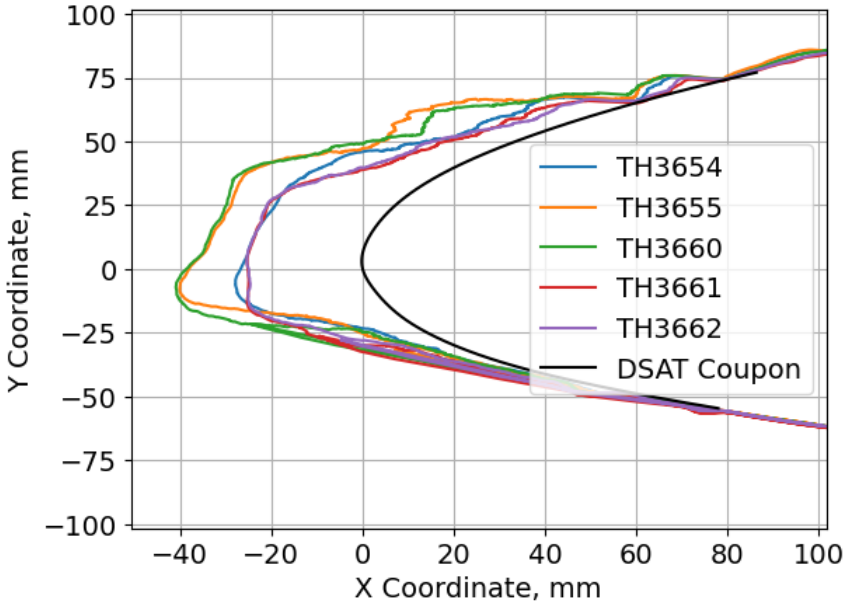

Fig. 19 Maximum combined cross section of the ice accretions used during the DSAT IRT campaign

VI. Conclusion

A new in-situ, hands free, ice adhesion methodology has been developed and tested in the GRC IRT with the goal of producing highly consistent results. To accomplish this, the Deformed Skin Adhesion Test was designed to produce the necessary surface tractions to induce delamination by using bending as the primary loading mechanism. Using finite element analysis, this test was studied to better understand the role of ice layer thickness and determine which opening modes dominate this test. It was found that this test is highly dominated by the normal opening stress (Mode I Opening) with all other stress components being an order of magnitude smaller. It was also found that for ice thicknesses beyond 10 millimeter, the DSAT is insensitive to the total ice layer thickness.

Instrumented with a one-axis load cell and a linear variable inductance transducer, the DSAT was installed into the leading edge of the hybrid CRM model and tested in the NASA Glenn Icing Research Tunnel. During this test campaign, the DSAT performed well and was able to produce consistent results across multiple days of testing, with the applied load for ice delamination showing more variability compared to the stiffness results.. The invariance of the results for sufficiently thick ice layers was confirmed, as well as the insensitivity to the test being conducted either after or during an icing spray. An anomaly was noticed regarding results from the first test conducted each day which was attributed to a change in the interfacial bonding state. This was discovered using differential image analysis to observe non-uniform behavior during the early stages of ice accretion. Overall, the DSAT performed very well and is a candidate for future testing over a larger range of icing times and conditions.

The next step for this work is to conduct finite element simulations with a focus on matching the force-displacement results gathered experimentally. This will allow for the stress state immediately prior to delamination to be calculated and the critical stress values determined. However, before this work can begin, the bonding state of the DSAT must be further explored along with an understanding of the driving mechanisms for the first run anomaly.

Acknowledgments

The author would like to thank the NASA Revolutionary Vertical Lift Technology project for their funding support. The author would also like to acknowledge Andrew Work and Andrew Jimenez for their efforts in the development and design of the deformed skin adhesion test coupon. Additionally, this work would not have been possible without the support from the members of the NASA Glenn Icing Branch during the test campaign along with the IRT staff and technicians for their efforts in making this test campaign a success.

VII.References

[1] A. Work and Y. Lian, "A critical review of the measurement of ice adhesion to solid substrates," *Progress in Aerospace Sciences,* vol. 98, pp. 1-26, 2018. doi:10.1016/j.paerosci.2018.03.001

[2] A. Laroche, M. J. Grasso, A. Dolatabadi and E. Bonaccurso, "Tensile and Shear Test Methods for Quantifying the Ice Adhesion Strength to a Surface," in *Ice Adhesion: Mechanism, Measurement and Mitigation*, Hoboken, NJ, Wiley, 2020. doi:10.1002/9781119640523.ch9

[3] S. Ronneberg, C. Laforte, J. He and Z. Zhang, "Comparison of Icephobic Materials through Interlaboratory Studies," in *Ice Adhesion: Mechanism, Measurement, and Mitigation*, Beverly MA, Schrivener, 2020, pp. 285-324. doi:10.1002/9781119640523.ch10

[4] N. Rehfeld, J.-D. Brassard, Y. Masafumi, H. Sakaue, M. Balordi, H. Koivuluoto, J. Mora, J. He, M.-L. Pervier, A. Dolatabadi, E. Asenath-Smith, M. Jarn, X. Hou and V. Stenzel, "Round-Robin Study for Ice Adhesion Tests," *Aerospace,* vol. 11, 2024. doi:10.3390/aerospace11020106

[5] A. H. Work Jr., "A Statistical Analysis of Impact Ice Adhesion STrength Data Acquired with a Modified Lap Joint Test," *AIAA AVIATION Forum,* 2020. doi:10.2514/6.2020-2801

[6] Y. H. Yeong, A. Milionis, E. Loth, J. Sokhey and A. Lambourne, "Atmospheric Ice Adhesion on Water-Repellet Coatings: Wetting and Surface Topology Effects," *Langmuir,* vol. 31, pp. 13107-13116, 2015. doi:10.1021/acs.langmuir.5b02725

[7] R. Douglass, "Effects of Strain Rate Variation on the Shear Adhesion Strength of Impact Ice," *Thesis,* 2019.

[8] A. Jimenez, "Design and Analysis of a Novel Deformed Skin Adhesion Test for Aircraft Icing," *Case West Reserve University*, 2021.

[9] E. N. Timko, L. E. King-Steen, J. F. Van Zante and W. J. Acosta, "NASA Glenn Icing Research Tunnel: 2019 Cloud Calibration Procedure and Results," no. NASA/TM-20205009045, 2021.

[10] S. Lee, A. Broeren and M. Potapczuk, "Comparison of Ice Shapes on Full-Chord and Truncated Swept Wing Models," *AIAA AVAITION*, 2021.
doi:10.2514/6.2021-2679

[11] J. J. Petrovic, "Mechanical properties of ice and snow," *Journal of Materials Science*, pp. 1-6, 2003.

[12] J. William, "The Fracture Mechanics of Delamination Tests," *Journal of Strain Analysis*, vol. 24, no. 4, pp. 207-214, 1989.

[13] C. Giuffre and R.-C. Chen, "Impact Ice Adhesion at NASA Glenn: Current Experimental Methods and Supporting Measurements," *SAE Technical Paper*, no. 2023-01-1444, 2023.
doi:10.4271/2023-01-1444

[14] A. H. Work, "Icing Formation Strains on Airfoil Skin," *AIAA AVIATION Forum*, 2021.
doi: 10.2514/6.2021-2688